

## Dislocation-toughened ceramics

### Authors:

Lukas Porz<sup>a\*</sup>, Arne Klomp<sup>a</sup>, Xufei Fang<sup>a</sup>, Ning Li<sup>b</sup>, Can Yildirim<sup>c</sup>, Carsten Detlefs<sup>c</sup>, Enrico Bruder<sup>a</sup>, Marion Höfling<sup>a</sup>, Wolfgang Rheinheimer<sup>a,d</sup>, Eric A. Patterson<sup>a,e</sup>, Peng Gao<sup>b</sup>, Karsten Durst<sup>a</sup>, Atsutomo Nakamura<sup>f,g</sup>, Karsten Albe<sup>a</sup>, Hugh Simons<sup>h</sup> and Jürgen Rödel<sup>a\*</sup>

- a) Technical University of Darmstadt, Department of Materials and Earth Science, Darmstadt, Germany
- b) Peking University, Beijing, China
- c) European Synchrotron Radiation Facility, Grenoble, France
- d) Forschungszentrum Jülich GmbH, Jülich, Germany
- e) U.S. Naval Research Laboratory, Materials Science and Technology Division, Washington DC, USA
- f) Department of Materials Physics, Nagoya University, Nagoya, Japan
- g) PRESTO, Japan Science and Technology Agency, Tokyo, Japan.
- h) Department of Physics, Technical University of Denmark, Kongens Lyngby, Denmark

\* Corresponding authors: porz@ceramics.tu-darmstadt.de, roedel@ceramics.tu-darmstadt.de

### Supplementary 1: Evidence for the absence of nucleation of dislocations in particular at crack tips.

Upon indenting a SrTiO<sub>3</sub> single crystal with a Vickers indenter both cracks and dislocations are generated. After indenting, dislocations can be revealed by etching with buffered HF. Some of the cracks are then clearly free of dislocations as shown in Figure S1a.

To more accurately demonstrate the absence of nucleation at a crack tip, SrTiO<sub>3</sub> was fractured in 4-point bending. After the fracture, the side surface was etched in buffer HF to reveal dislocations as etch pits. Figure S1b verifies that no new dislocations were generated by the crack where the crack planes lies in the third dimension in so that the dislocation density as a function of distance from the fracture path can be observed.

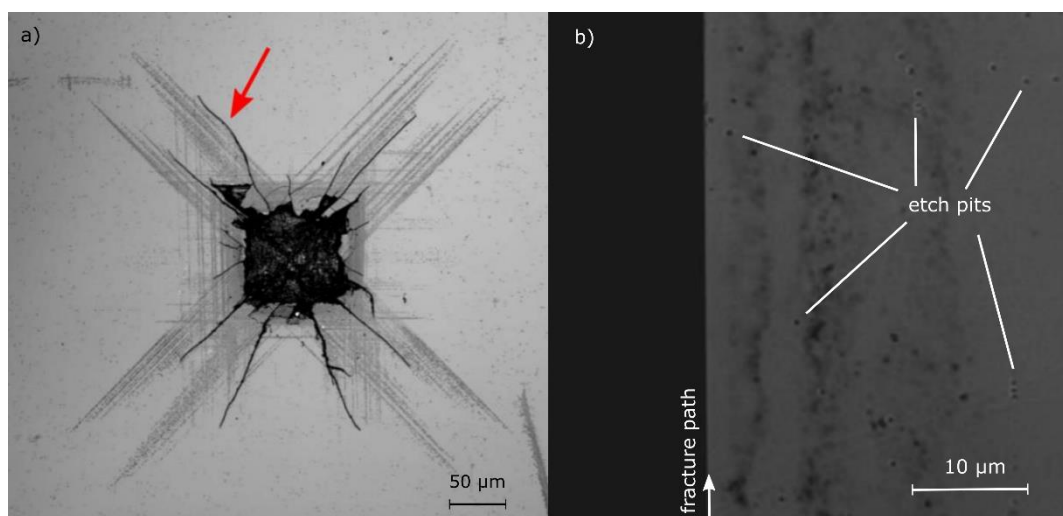


Figure S1: Evidence for the absence of nucleation of dislocations at crack tips in SrTiO<sub>3</sub>. a) Vickers indent with 19.62 N on a (100) surface where cracks are visible in areas without increased dislocation density. b) Side view of a fracture path of a SrTiO<sub>3</sub> single crystal showing no increased dislocation density at the fracture path nor a gradient as function of the distance from the crack path.

### Supplementary 2: Conventionally sintered ceramics are quasi dislocation-free

Undoped polycrystalline SrTiO<sub>3</sub> was sintered in pure oxygen at 1425°C for 1 hour followed by a holding time of 15 h at 1350°C. More details on the synthesis can be found in the literature<sup>1</sup>. A sample was prepared by conventional TEM sample preparation. Images were taken using the JEOL JEM-1000k RS operated at 1 MV. Only three dislocations were found in 133 grains. This corresponds to a dislocation density of  $5 \cdot 10^9 \text{ m}^{-2}$ .

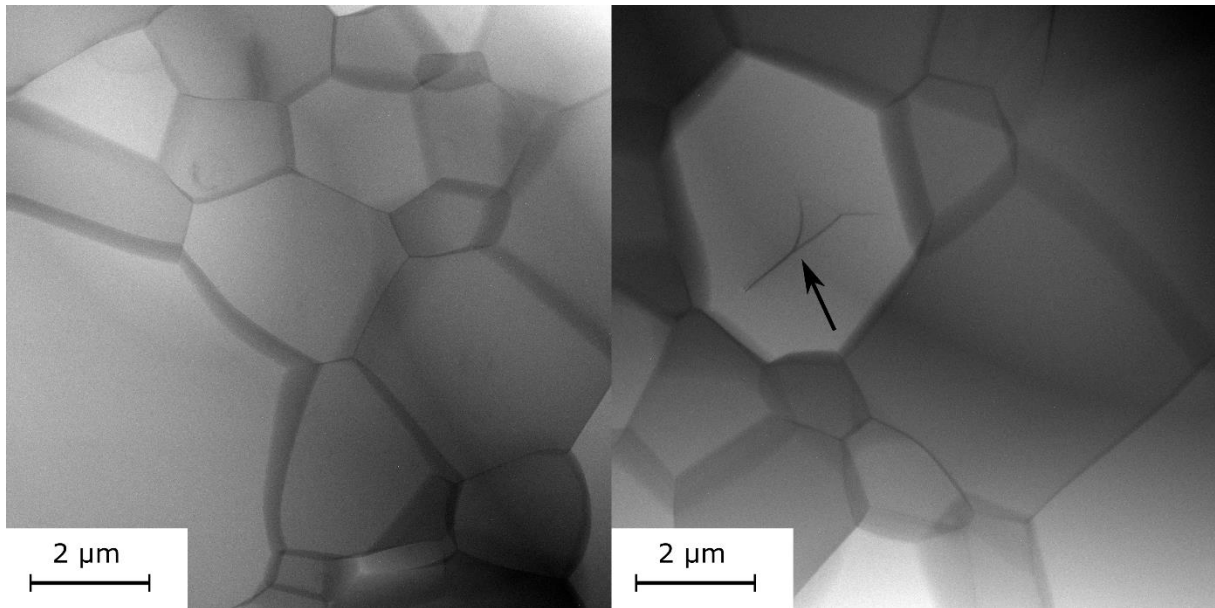


Figure S2: STEM images of conventionally sintered SrTiO<sub>3</sub> with next to no dislocations. A dislocation that was found is marked with an arrow.

### Supplementary 3: Video of all slip bands with explanation

The video provides firstly the near-field topo-tomography<sup>2</sup> images with a 360° rotation. Later, a far-field image with increased magnification is highlighted. The sample is tilted around the direction of the slip bands allowing to observe them under varying shallow angle. This helps identifying the 3D nature of the observed objects. Image artifacts, slip bands and individual features are indicated and labeled in the video.

A section from video 3 is illustrated as an image in Figure S3. Slip bands, image artifacts from an unpolished sample surface, cross slip points and individual dislocations are highlighted.

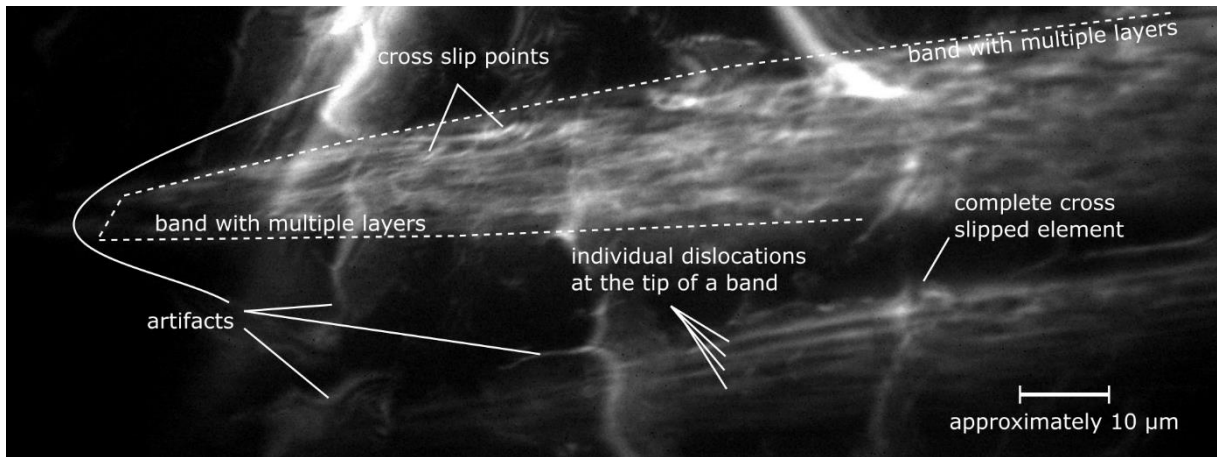


Figure S3: Explanation of exemplary features observable from topo-tomography images in dark-field x-ray microscopy. The marked artifacts arise from the scratches of the unpolished surface.

Supplementary 4: quantitative dark-field x-ray image analyzing the lattice rotation (mosaicity) around slip bands.

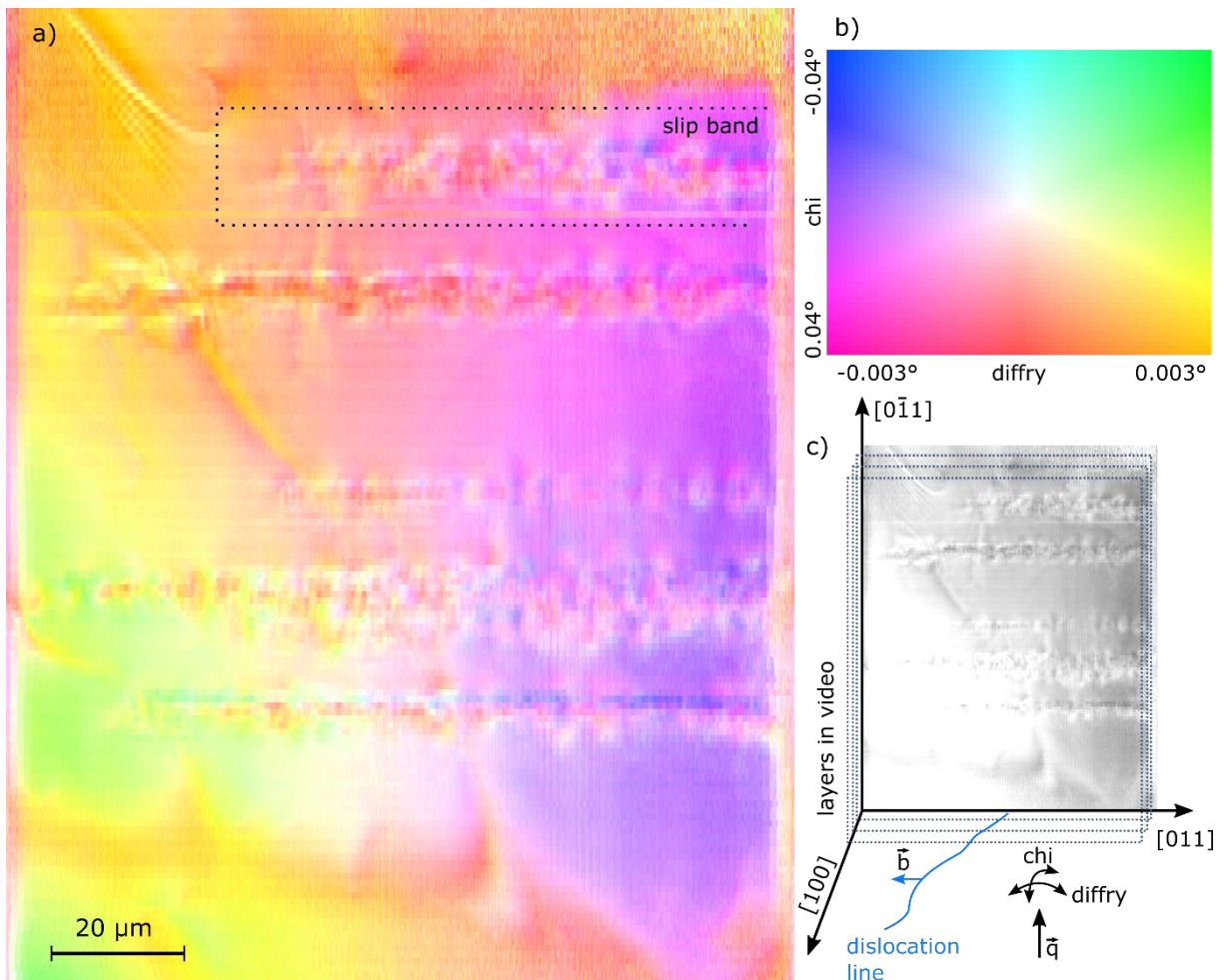


Figure S4: Map of local lattice tilt around slip bands in a  $\text{SrTiO}_3$  single crystal composed of 2048 data points in horizontal direction and 145 data points in vertical direction. a) Mosaicity (local lattice tilt) around a set of slip bands. b) Color key quantitatively relating the color to the instrument tilt angle  $\chi$

and diffraction. C) Sketch of the Burgers vector, the dislocation line, the diffraction vector and the two tilt angles. 2048 layers of this image are combined into supplemental video 5.

#### Supplementary 5: Video of layers with lattice tilt

In supplemental video 5, the volume is presented in slices which scan from the sample bottom to the sample top. Each voxel contains quantitative information about the local lattice tilt. Slip bands are clearly visible. For better understanding, please refer to supplemental video 6 which images the same sample volume but using far field topo-tomography.

#### Supplementary 6: Layered 3D reconstruction (video)

The data resulting in Figure S4 is visualized in 3D while the image is rotated around arbitrary axes. Voxels including dislocations are visible while voxels without dislocations are not. However, with the current experimental data a clear physical definition of which voxel contains how many dislocations in contrast to signals caused by artifacts is not robustly feasible. Hence, the 3D structure of the slip bands is recognizable but minor experimental improvements are necessary to allow for an exact 3D reconstruction.

#### Supplementary 7: Visualization of the data from all 145 layers into a 3D reconstruction

The contrast is significantly weaker when imaging in 145 layers as compared to the image in supplemental video 5 where the whole volume is imaged at once. Shaded in orange, the slip bands can be clearly identified in the displayed volume section. The slip bands can be nicely reconstructed in 3D. However, the individual dislocations cannot be discerned. As illustrated in the second image, with the chosen imaging conditions, the noise level is in many cases higher than the intensity of the dislocations. Please note that a sub-volume was chosen to avoid artifacts at the sample surface.

It nevertheless proves the concept that 3D reconstruction can be done with dark-field x-ray microscopy. Improvements for future studies should be:

- All sample surfaces should be polished to remove any unwanted distorted regions.
- Smaller layer spacing, e.g. less than 200 nm, should be applied.
- Choose the imaging layer in a way that the dislocation line vector is as close as possible to perpendicular to the imaging layer plane.
- Increases in resolution will be beneficial.

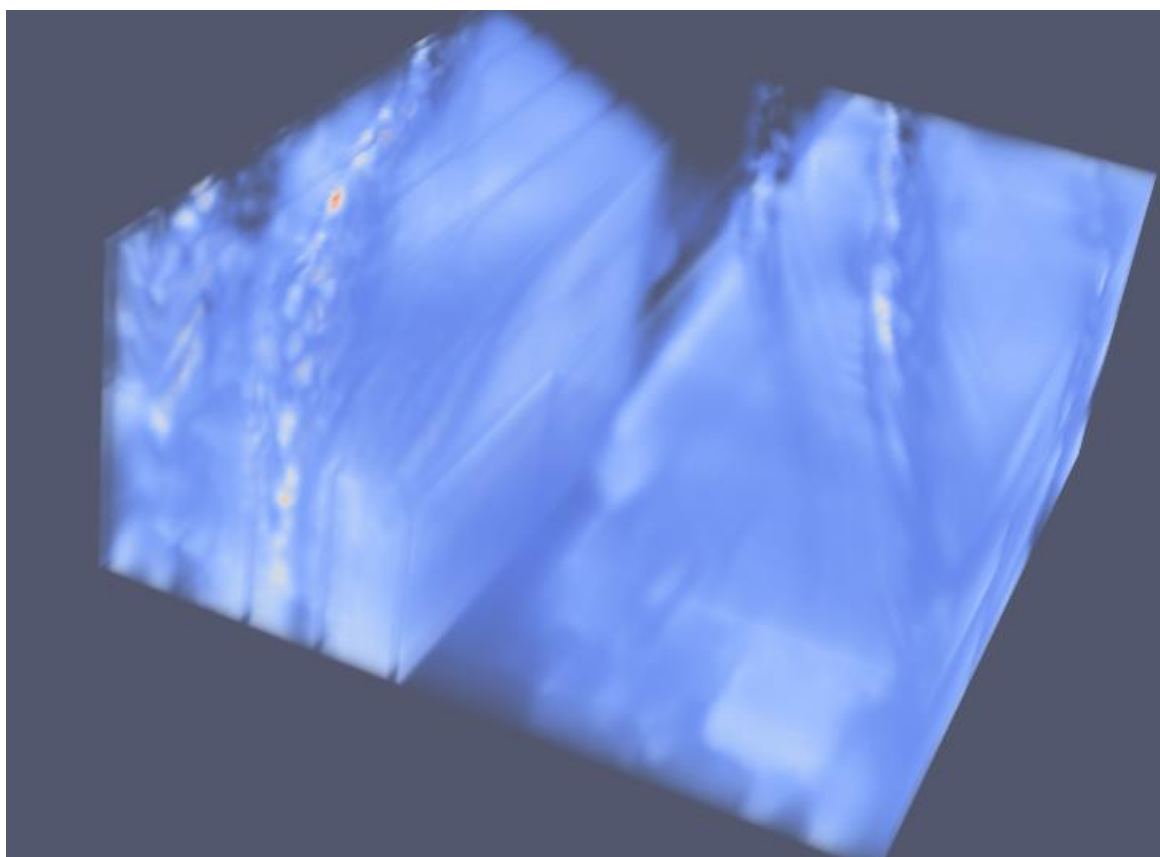
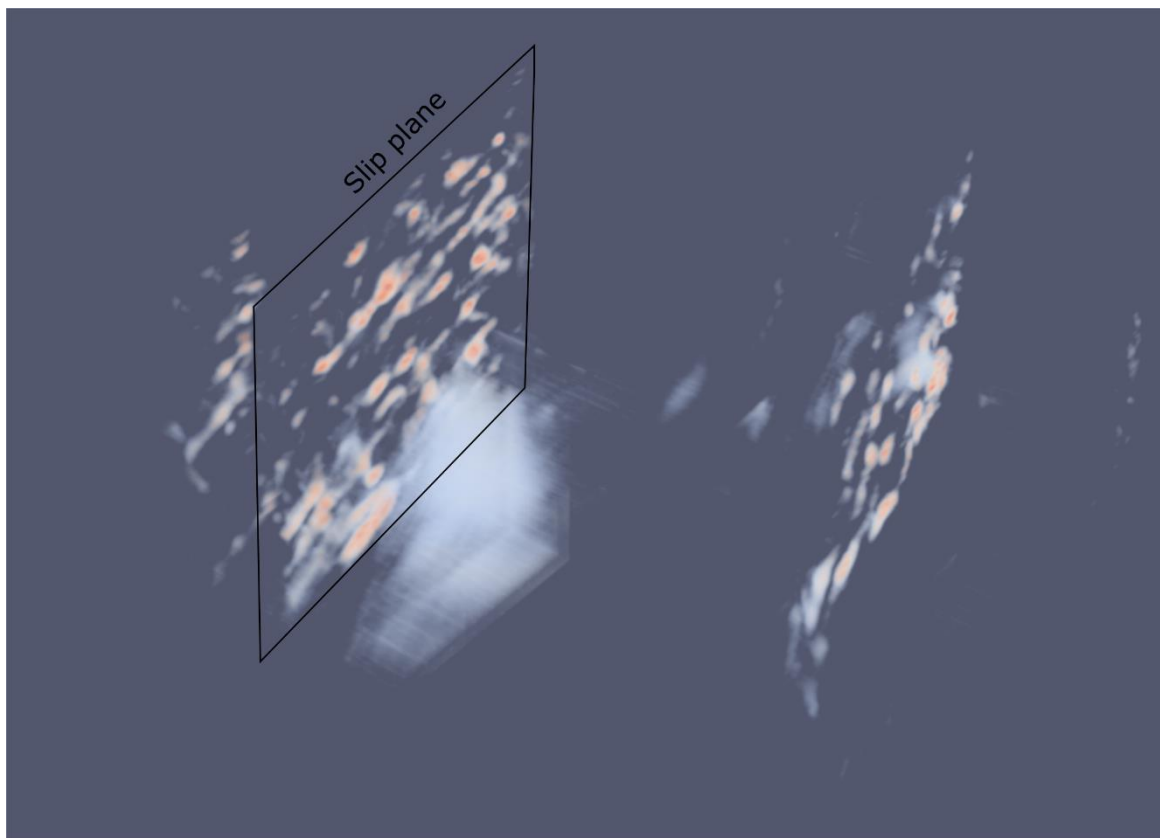


*Figure S5: Visualization of 3D data obtained from dark-field x-ray microscopy with two different conversions from raw signal to displayed contrast. As indicated, slip planes can be identified but the contrast is not sufficient to visualize individual dislocations.*

### Supplementary 8: High voltage electron microscopy images

A  $\text{SrTiO}_3$  single crystal was deformed by 2% at room temperature. A TEM sample was prepared by conventional TEM sample preparation and images were taken using the JEOL JEM-1000k RS operated at 1 MV. Individual dislocations can be identified. Their Burgers vector was confirmed by aligning Burgers vector and diffraction vector.

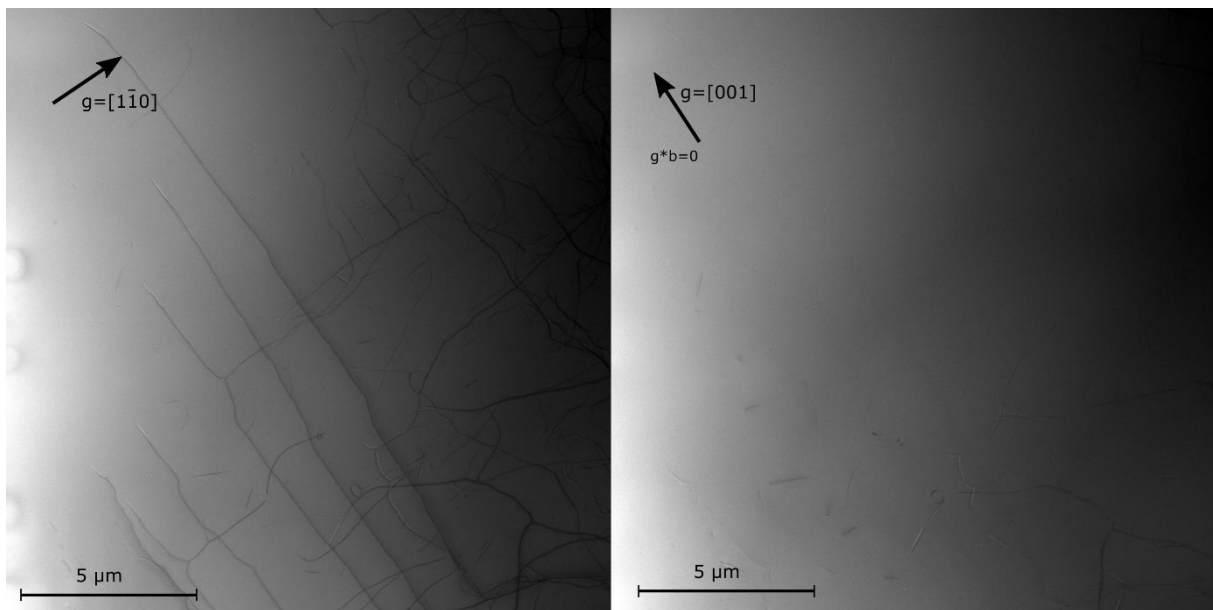


Figure S6: High voltage electron microscopy images of a  $\text{SrTiO}_3$  single crystal deformed by 2% at room temperature.

Supplementary 9: Overview over TEM images of dislocations

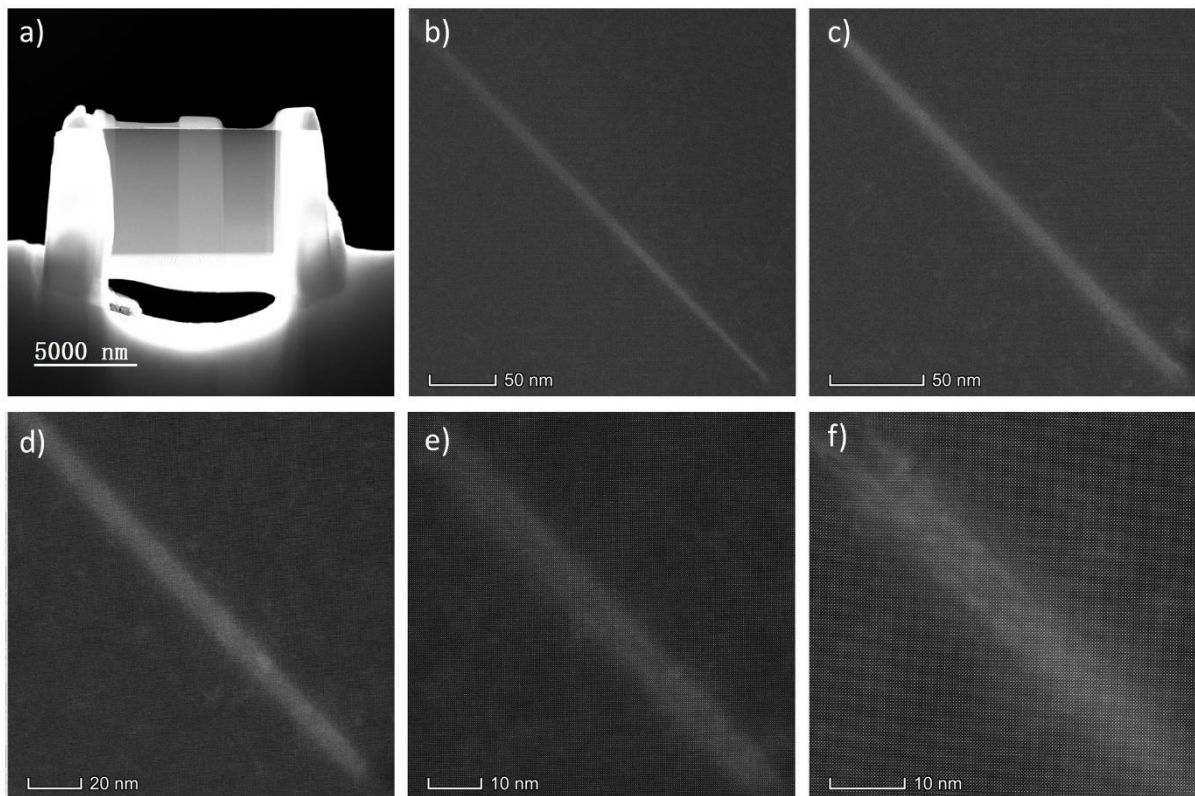


Figure S7: Low magnification STEM-HAADF images of SrTiO<sub>3</sub>. a) The HAADF image of TEM sample prepared by FIB, preventing the influence of mechanical polish. b-f) Dislocations (pairs) with different length and width found in the sample.

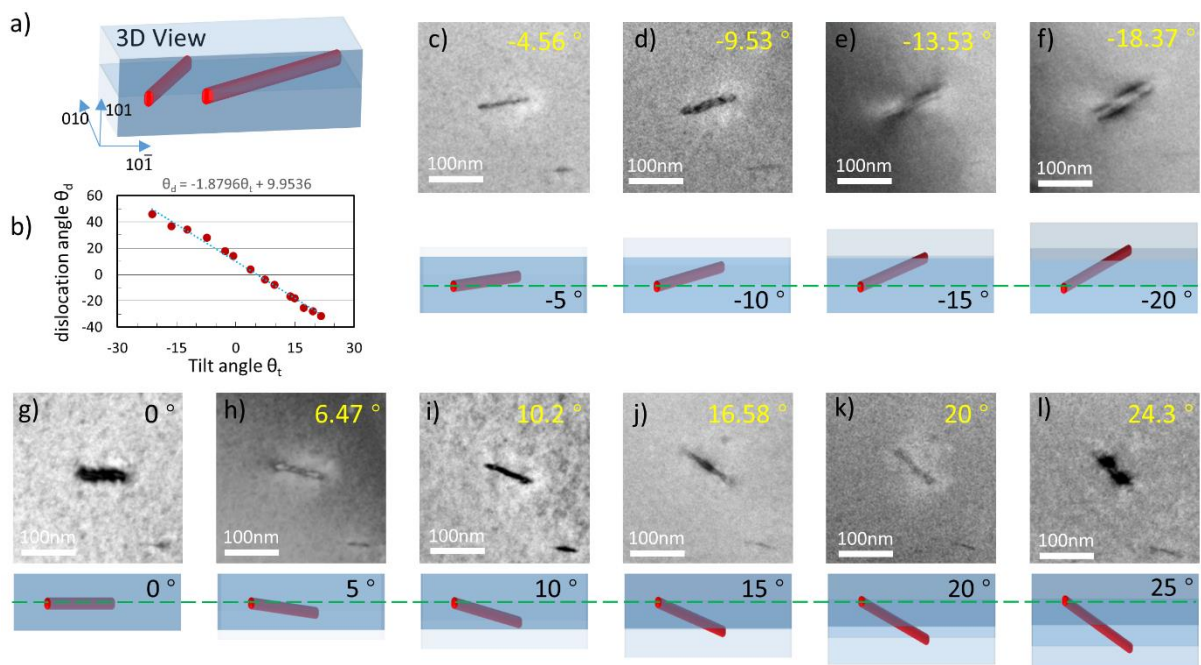


Figure S8: 3D model of the dislocation band. a) The 3D model of dislocation lines across the SrTiO<sub>3</sub> crystal. b) The experimentally measured dislocation line angle ( $\theta_d$ ) as a function of the sample tilting angle ( $\theta_t$ ). This data demonstrates that  $\theta_d$  has a linear relationship with  $\theta_t$ . c-l) Comparison of the dark-field TEM images and the model results at different tilt angles.

### Supplementary 10: Explanation of the climb-dissociated position

With sufficient thermal activation, the two partial dislocations can relax into a configuration where the elastic strain energy is minimized. This is achieved when the tensile stress region of one partial dislocation overlaps with the compressive stress region of the other partial.

In this configuration, the partial dislocations are no longer in the same plane and hence the trailing partial cannot annihilate the stacking fault produced by the movement of the leading partial. This renders them much less mobile<sup>3,4</sup>.

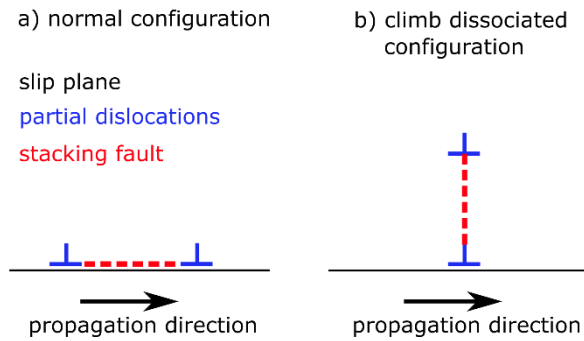
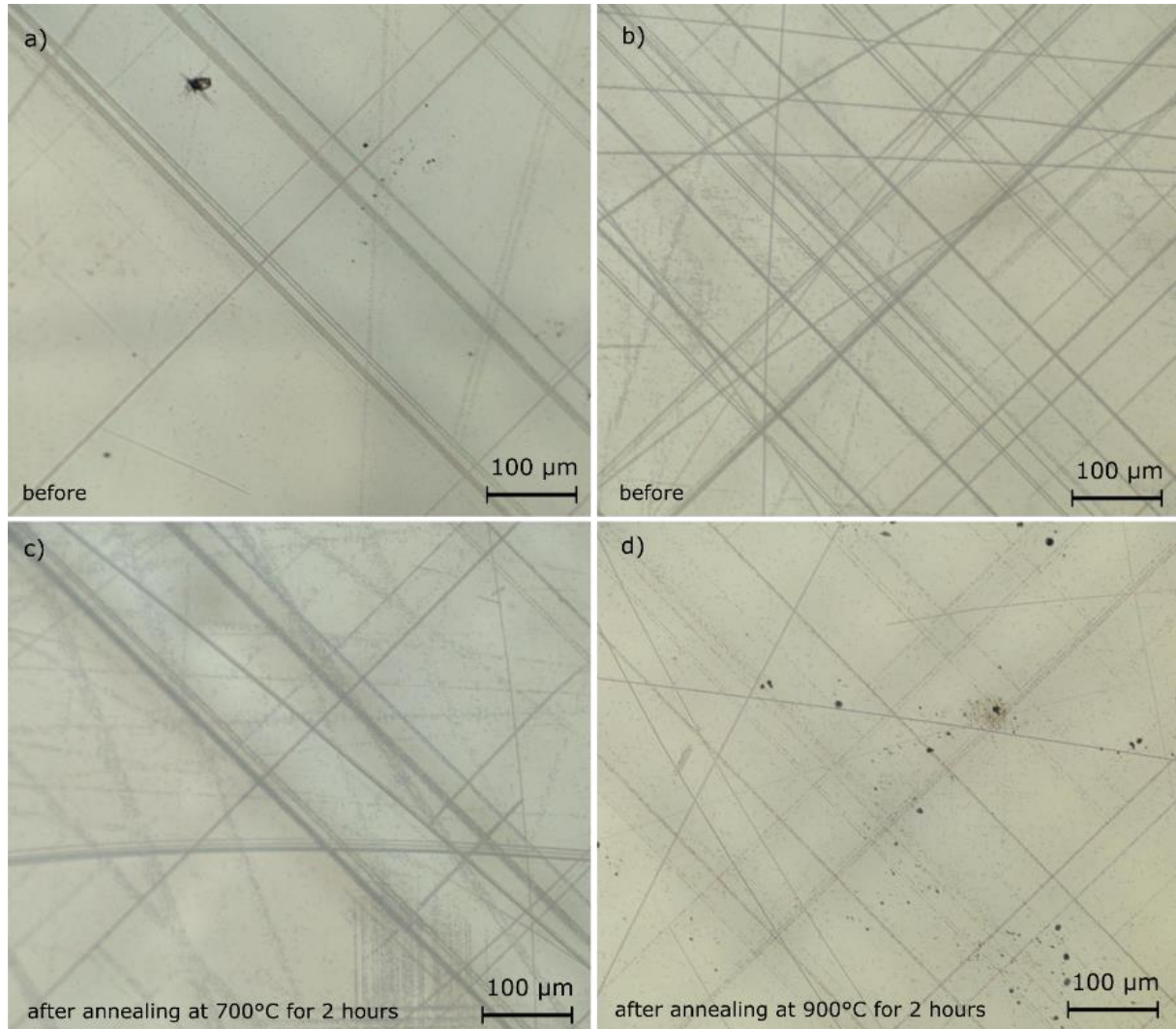


Figure S9: Schematic illustrating climb dissociation.

### Supplementary 11: Evidence for dislocation annihilation around 850°C

Thermal stability of the slip bands was tested in simple annealing experiments. Slip band structure was fabricated and etched on one side. After annealing, the other side was etched as well. Focusing the microscope on top and bottom plane of the transparent crystal allows comparing the etch pits pattern formed before and after the annealing step.



*Figure S10: Experimental evidence for dislocation annihilation at elevated temperature. A sample was produced according to Porz et al.<sup>5</sup> and cut into 700 μm thin slices. One side was etched. Then 2 hour annealing treatments were done at 700°C and 900°C (and other temperatures which are not shown). After the annealing, the other side was etched. Due to the transparency of the crystals, an optical microscopy image of the exact same location could be obtained by focusing on the top and the bottom surface. Hence, the dislocation structure before and after annealing can be contrasted.*

### Supplementary 12: Molecular dynamics

In order to assist the understanding of our experimental findings we conducted molecular dynamics simulations. In the following we briefly summarize the simulation framework and the models employed. Next the setup of the simulation, its boundary and experimental conditions are described.

After that we suggest the emission of dislocations at stress concentrations and that dislocations are able to easily propagate within the crystal. Even in a perfect crystal, dislocations are prone to creating other defects in the crystal structure. Such defects (also called *debris*) assist in the multiplication of dislocations even on planes that are not parallel to the original direction of dislocation propagation.

## Method

We chose the classical molecular dynamics (MD) method for our simulations because it can treat a sufficient volume of material (i.e. number of atoms) to accommodate the elastic as well as possible electrostatic fields of dislocations while at the same time retaining the discrete atomic nature of solids. For reasons of comparison with the experiment on SrTiO<sub>3</sub> single crystals we selected the same material here. The interatomic interactions are accounted for by a Born-Meyer type potential that includes fixed effective ionic charges as designed by ref.<sup>6</sup>. As simulation software we use LAMMPS (<http://lammps.sandia.gov>) on the Lichtenberg high performance computer of the Technical University of Darmstadt<sup>7</sup>.

## Setup and Analysis

Slabs of stoichiometric single crystalline SrTiO<sub>3</sub> have been created by aligning the slab axes with the principle crystallographic axes and a sharp notch has been applied at one side by removal of atoms (for geometry see Figure S11). The simulated cell is periodic along the direction of applied stress/strain and the direction which the dislocations lines are expected to follow. The latter of the two is chosen to be only 5 unit cells thick because dislocations are expected to be quasi-infinite in line direction and especially in order to reduce computational load. In total such simulations contain approx. 6.5 million atoms. We note that such a setup probably suppresses the observation of kinked dislocation lines. Also, since the cell is continuously relaxed along this direction the dislocation line tension might be reduced. The third direction is also modeled with periodic boundary conditions but sufficient vacuum space (approx. twice the corresponding slab size) is inserted to prevent self-interaction along this direction. Loading is applied along the vertical direction in Figure S11 using a constant engineering strain rate. Analysis of the results, especially the identification of dislocation structure, is to a large extent assisted by the software OVITO (<https://www.ovito.org>) and the dislocation extraction algorithm<sup>8,9</sup>.

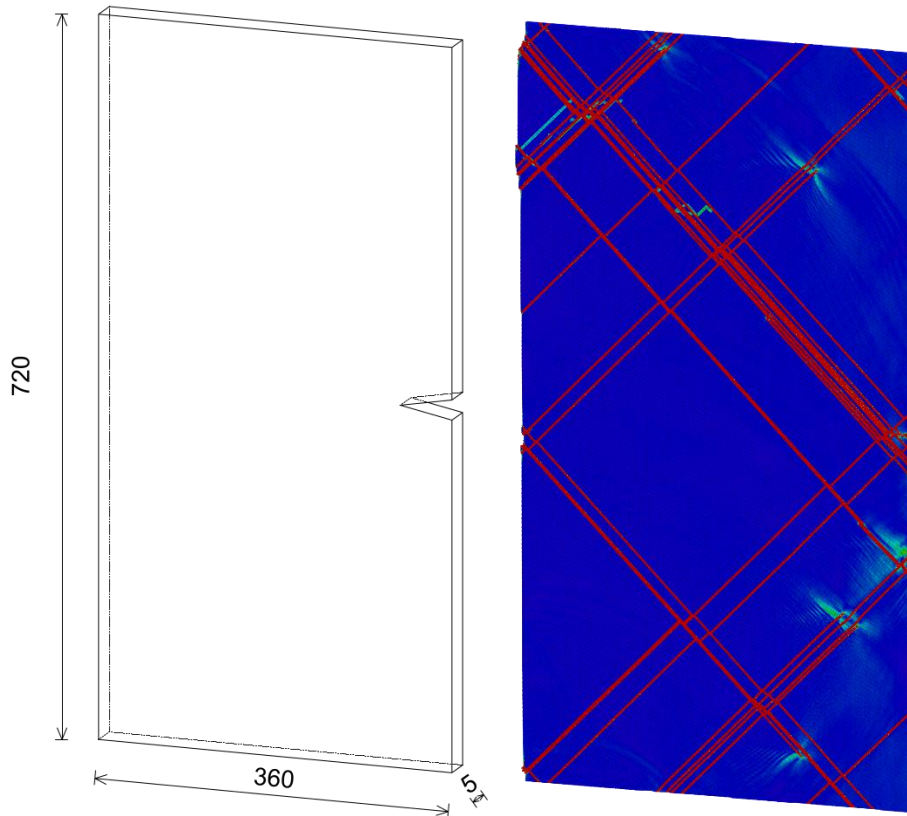


Figure S11: Overview of the simulation sample. On the left the dimensions of the initial sample are given in number of  $\text{SrTiO}_3$  unit cells. On the right the sample is displayed after the compression simulation with the color coding as described below. Strain is applied in the vertical, i.e. the longest direction.

### Compression at high strain rate

As described above a notched single crystalline slab is created and equilibrated at 10 K. This is close to a static calculation but gives the system some energy to leave shallow local minima while preventing thermally activated processes. The slab is then prestrained by 1.8 %. This state is equilibrated for 20 000 steps with a time step of 2 fs without observation of any defects created at the notch tip. Strain is successively applied with a loading rate of  $0.4 \text{ \AA ps}^{-1}$  (i.e. strain rate of  $1.42 \times 10^8 \text{ s}^{-1}$ ). The first plastic yielding occurs at a compressive strain of 2.3 % by emission of the first dislocation partial from the notch. The dislocations observed here are of identical type as in the experiment, i.e. the  $\langle 110 \rangle \{110\}$  family. They travel at a velocity that is close to the speed of

sound in the material. In fact using the 0 K isotropic elastic parameters of the model material the longitudinal speed of sound is calculated with

$$v_{long} = \sqrt{\frac{E(1-\nu)}{\rho(1-\nu-\nu^2)}}$$

providing a value of  $8022 \text{ ms}^{-1}$ . Observation of the travelling dislocations in the simulations gives an average velocity of approx.  $2130 \text{ ms}^{-1}$ . Although the crystal is set up as a perfect single crystal and temperature is set to 10 K only, dislocations do rarely transverse the crystal in a straight line. Three different types of processes have been identified that lead to the creation of new defects.

- A) Without apparent reason, the dislocations change plane and then propagate parallel to their original direction (see Figure S12). Such spontaneous climbing processes (temperature is too

low for thermal activation) leave behind defects in the crystals, mainly stoichiometric agglomerates of vacancies. Such a behavior is expected from dislocations moving at high velocity<sup>10</sup> and similar processes have been demonstrated in other simulation works as well, e.g. ref. <sup>11</sup>. Even within short distances of dislocation motion several such processes may occur. An exemplary detailed analysis of a climb process verifies that the partials climb after one another.

- B) As traveling partial dislocations climb (or potentially cross glide), they can create *debris* (here: vacancies) and multiply. Figure S13 demonstrates how a dislocation multiplies by climb of one partial and consecutive nucleation of new partials to avoid stacking faults. It should be noted that this process seems to be in part driven by the comparably high stacking fault energy in this material<sup>12</sup>.

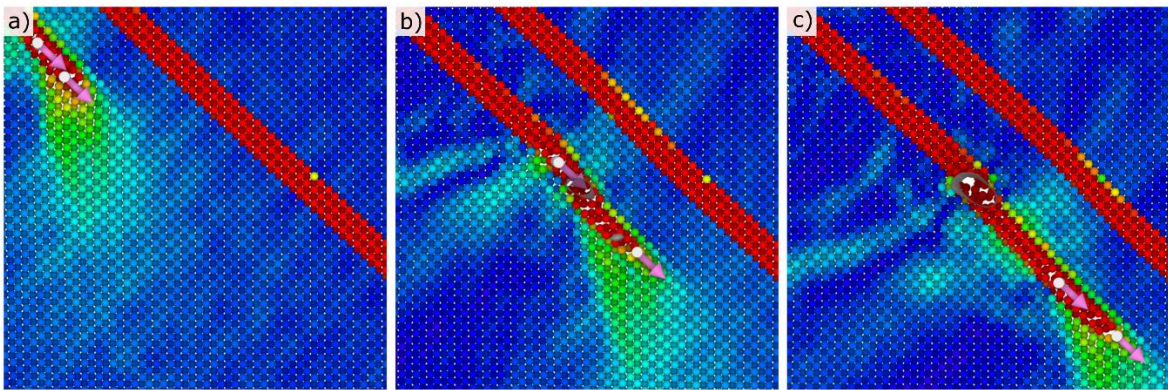


Figure S12: Snapshot of a climbing dislocation. Atoms are color coded according to the shear strain they have experienced relative to the start of the simulation, whereby red indicates high and blue indicates low values. The dislocation lines are represented in white and Burgers vectors in pink (scaled by a factor of 4 for easier visibility.). A surface mesh on defects is shown in gray. In the top right part of each image one can see the track of a previously moved dislocation. In the pictures from left to right we can observe (a) two partials moving from top left to bottom right; (b) the first partial dislocation has climbed one unit cell and the second partial is still on its original plane; (c) the two partials have climbed leaving behind a step in their track and an agglomerate of vacancies.

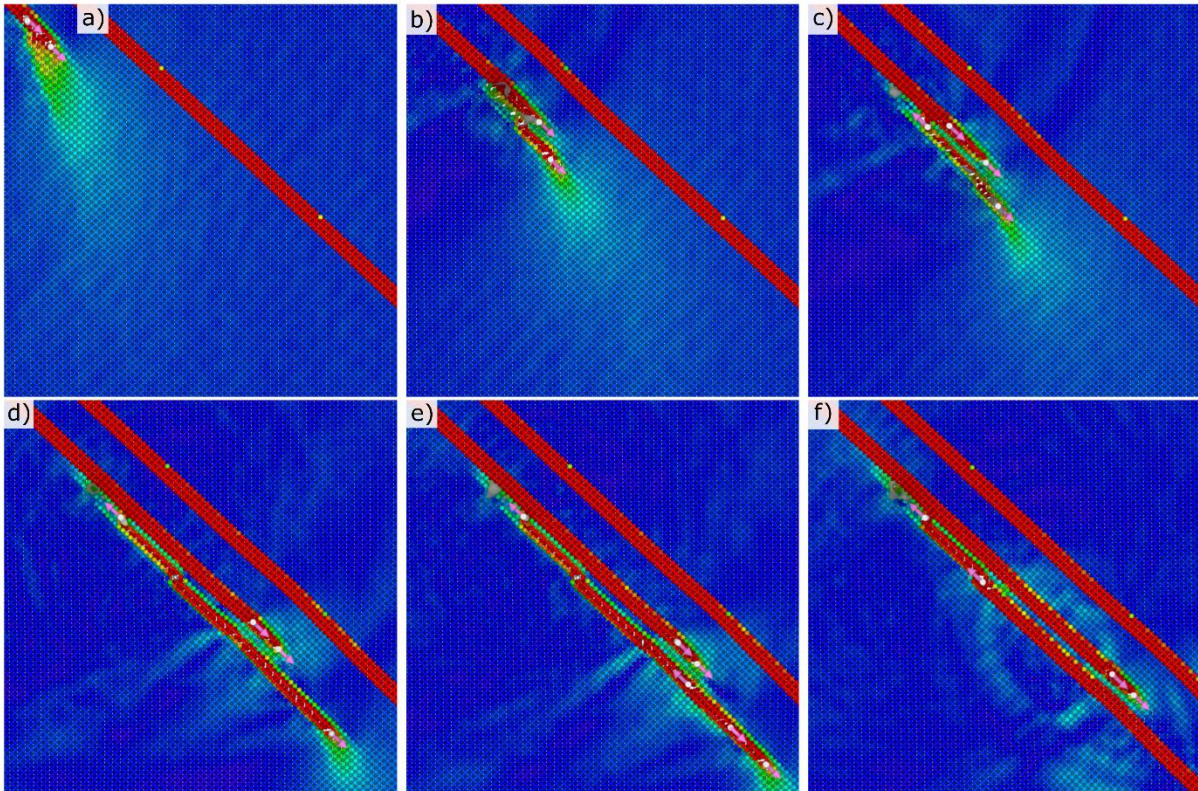


Figure S13: Dislocation multiplication on a parallel glide system. Color coding as in Figure 12. A pair of two partials move inside their glide plane (a) when the first partial changes plane by a climb process (b). Moving two partials in separate glide planes creates extended stacking faults which is energetically unfavorable. Instead two new partials spawn (c) so that there is one complete set on the original plane and an antagonistic pair on the new plane. According to the forces acting on the dislocations, the two corresponding partials move together, while the two antagonistic partials separate from each other creating an extended stacking fault (d). As the stacking fault becomes too large, again two new partials nucleate in the stacking fault completing the dislocations (e) and subsequently associate with their corresponding partial to minimize stacking fault energy (f).

We note that the stresses acting to nucleate new dislocations inside the material are a superposition of externally applied stresses and internal stresses originating from other defects. Internal stress fields are in particular created by other dislocations. As there is a dislocation density ranging from  $7 \times 10^{13} \text{ m}^{-2}$  to  $3 \times 10^{14} \text{ m}^{-2}$ , which is close to the real dislocation density in dislocation bands of the experimental sample, the elastic fields of dislocations overlap. A linear elastic approach estimated the additional internal stresses created by certain dislocation arrangements to be in the GPa range. The high dislocation density thus enhances the multiplication and nucleation of further dislocations.

### Compression at low strain rate

In order to verify that the processes leading to defect creation are not an artifact of the high loading rates we conduct the same experiment but with lower strain rate<sup>10,11</sup>. The simulation sample has been prepared in exactly the same way as described in the previous section. The difference lies in the loading rate which is now chosen to be  $0.04 \text{ \AA ps}^{-1}$  corresponding to an engineering strain rate of  $1.42 \times 10^7 \text{ s}^{-1}$ , i.e. ten percent compared to the previous experiment. Again dislocations are emitted from the notch and surface faults, this time starting from strains of 2.0 % (as expected a lower strain rate leads to lower values for strain and stress).

Essentially, the behavior of the dislocations under reduced loading rate features no significant difference to fast loading. Apart from moving slightly slower they still create the same defects in the crystal as described above. Of course the applied strain rate is still far from experiment but lower strain

rates are prohibited by the enormous computational demand. Within the limits tested here we can state that the dislocation behavior described above seems not to depend very strongly on loading rate.

### **Climb-dissociated dislocations**

In order to rationalize the easy climb of dislocations the stability of the  $\langle 110 \rangle \{100\}$  edge dislocations that dominate the above simulations is reviewed. As already indicated by Hirel et al. this dislocation type tends to climb dissociate at elevated temperatures [9]. We base our results (see Figure 2h of the main publication) on comparison of the potential energy of different dislocation configurations. The simulated system is an orthogonal slab of stoichiometric  $\text{SrTiO}_3$  with two unit cell thickness along the dislocation line ( $[001]$  direction) and  $160 \times 160$  unit cells cross-section ( $[110]$  and  $[\bar{1}\bar{1}0]$  directions). Two antiparallel full dislocations are introduced by cutting out an atomic plane of thickness  $a \langle 110 \rangle$  and carefully relaxing the system. Dislocations created in such a way are not charge balanced, i.e. one dislocation has excess oxygen while the other is oxygen deficient. Transferring half of the oxygen atoms that terminate one dislocation to the other dislocation balances the charge and reduces energy significantly (process analog to Marrocchelli et al. <sup>13</sup>). Note that the as-created full dislocation spontaneously glide dissociates while the charge balanced configuration does not.

For both systems, as-created and charge balanced, climb dissociation is modeled by decomposing the fully cut plane into two planes of thickness  $a/2 \langle 110 \rangle$  and shifting them relative to each other. The potential energies for all configurations can then be compared directly since the number of atoms remains the same. In addition, size convergence tests with simulation cell cross-sections of  $200 \times 200$  unit cells and  $300 \times 300$  unit cells have been conducted providing equal results. From the graph of potential energy over climb dissociation distance (see Figure 2h of the main publication) it can be ascertained that the climb-dissociated configuration is more stable than the as-created glide-dissociated as well as the charge balanced full dislocation configuration. Therefore, it is apparent that the dislocations have a strong tendency to climb. In a dynamic simulation of compression this climb interferes with the dislocation glide motion and leads to the observed defects.

### [Supplementary 13: Videos from Molecular dynamics simulation.](#)

The videos highlight the simulation results described in detail in supplementary information 14.

### [Supplementary 14: Dislocation density induced by the dislocation-inducing polishing procedure](#)

The dislocation density was determined by counting the number of dislocations in a specific area of electron channeling contrast images presented below. The channeling contrast using a BSE detector is used to visualize dislocations.

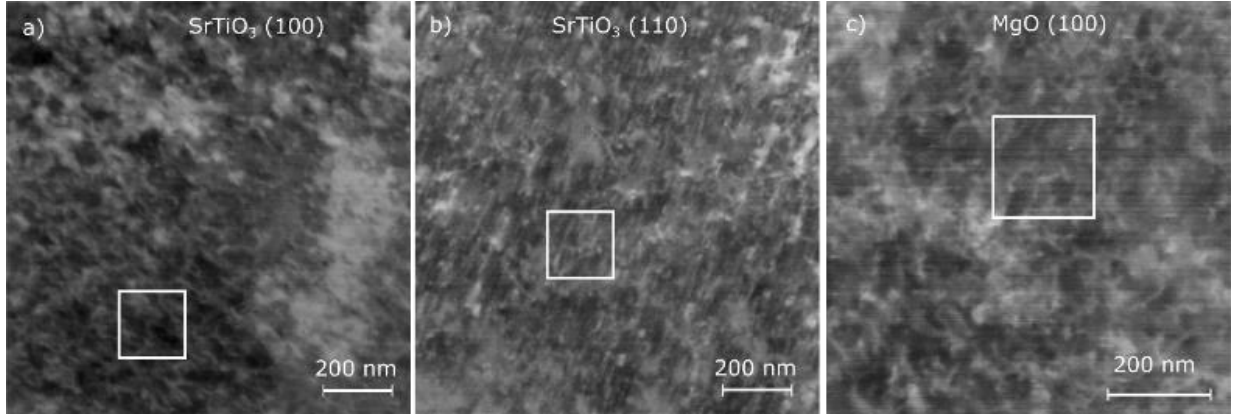


Figure S14: Electron channeling contrast images with view direction onto the treated surface used to calculate the dislocation densities. As example for the dislocation density evaluation a guide in form of a  $200 \times 200 \text{ nm}^2$  sized square is marked. In this square, in a) 17 dislocations can be found and a density of  $\rho = 4.25 \cdot 10^{14} \text{ m}^{-2}$  can be calculated. In b) 14 dislocations are identified ( $\rho = 3.5 \cdot 10^{14} \text{ m}^{-2}$ ), in c) 15 dislocations are counted ( $\rho = 3.75 \cdot 10^{14} \text{ m}^{-2}$ ). When averaging the dislocation density over larger regions for better statistics, the density is consistently computed at about  $5 \cdot 10^{14} \text{ m}^{-2}$  for both  $\text{SrTiO}_3$  and  $\text{MgO}$ .

#### Supplementary 15: Nanoindentation

The purely elastic relation between the load  $P$  and displacement  $h$  can be described by the Hertzian solution<sup>14</sup>:

$$P = \frac{4}{3} E_r \sqrt{R} h^{3/2} \quad (\text{S1})$$

Using the load-displacement curves one can fit the tip radius  $R = 80 \text{ nm}$  as used in the current work. The reduced modulus  $E_r$  is calculated from the elastic modulus and Poisson's ratio of the indenter and the specimen:

$$\frac{1}{E_r} = \frac{1 - \nu_i^2}{E_i} + \frac{1 - \nu_s^2}{E_s} \quad (\text{S2})$$

where  $E_i = 1140 \text{ GPa}$ ,  $\nu_i = 0.07$  for the diamond tip, and  $E_s = 264 \text{ GPa}$ ,  $\nu_s = 0.237$  for  $\text{SrTiO}_3$ <sup>15</sup>.

The pop-in load,  $P_{pop-in}$ , can be converted to a maximum shear stress,  $\tau_{max}$ , beneath the indenter during deformation. This critical shear stress represents the shear strength of the material, which is given by<sup>14</sup>:

$$\tau_{max} = 0.31 \left( \frac{6E_r^2}{\pi^3 R^2} P_{pop-in} \right)^{1/3} \quad (\text{S3})$$

#### Supplementary 16: Crack tip toughness evaluation by crack tip opening displacement

Macroscopic indentation to introduce cracks was performed separately using a Vickers tip and 0.1 N load. The crack tip toughness of short radial indentation cracks was quantified by determining the crack

opening displacement as function of distance to the crack tip in a scanning electron microscope at magnification of 100,000 times. Vickers indentations of 0.1 N load were placed into either pristine surfaces or surfaces with high dislocation density and then sputtered with carbon. About 24 hours after indentation the crack opening profile was recorded and the following equation used.

$$u = K_0 * \frac{E}{1 - \nu^2} * \sqrt{8x/\pi}$$

It relates crack tip toughness  $K_0$  to the half-opening  $u$ , distance to the crack tip,  $x$ , and elastic modulus,  $E$  as well as the Poisson's ratio  $\nu$ <sup>16,17</sup>. In detail, note that the crack is at equilibrium at the time of pop-in, but can be subject to subcritical crack growth in the 24 hours before quantification of the crack opening displacement. Strictly speaking, the crack tip stress intensity factor thus obtained provides a point on the velocity – stress intensity ( $v$ - $K$ ) curve, slightly below actual fracture toughness<sup>18</sup>. However, the ratio of fracture toughness between pristine and dislocation-toughened sample is expected to not be affected.

High resolution SEM images were acquired using the MIRA3-XMH SEM (TESCAN, Brno, Czech Republic) equipped with a 4-quadrant solid state BSE detector (DEBEN, Woolpit, UK). SEM images were simultaneously recorded with in-lens secondary electron (SE) detector and in-lens backscattered electron detector (BSE) using a magnification of 100,000 and a working distance of 3 mm. In the BSE image, the sputtered carbon to form a conductive surface is transparent which then eliminates potential shadowing effects.

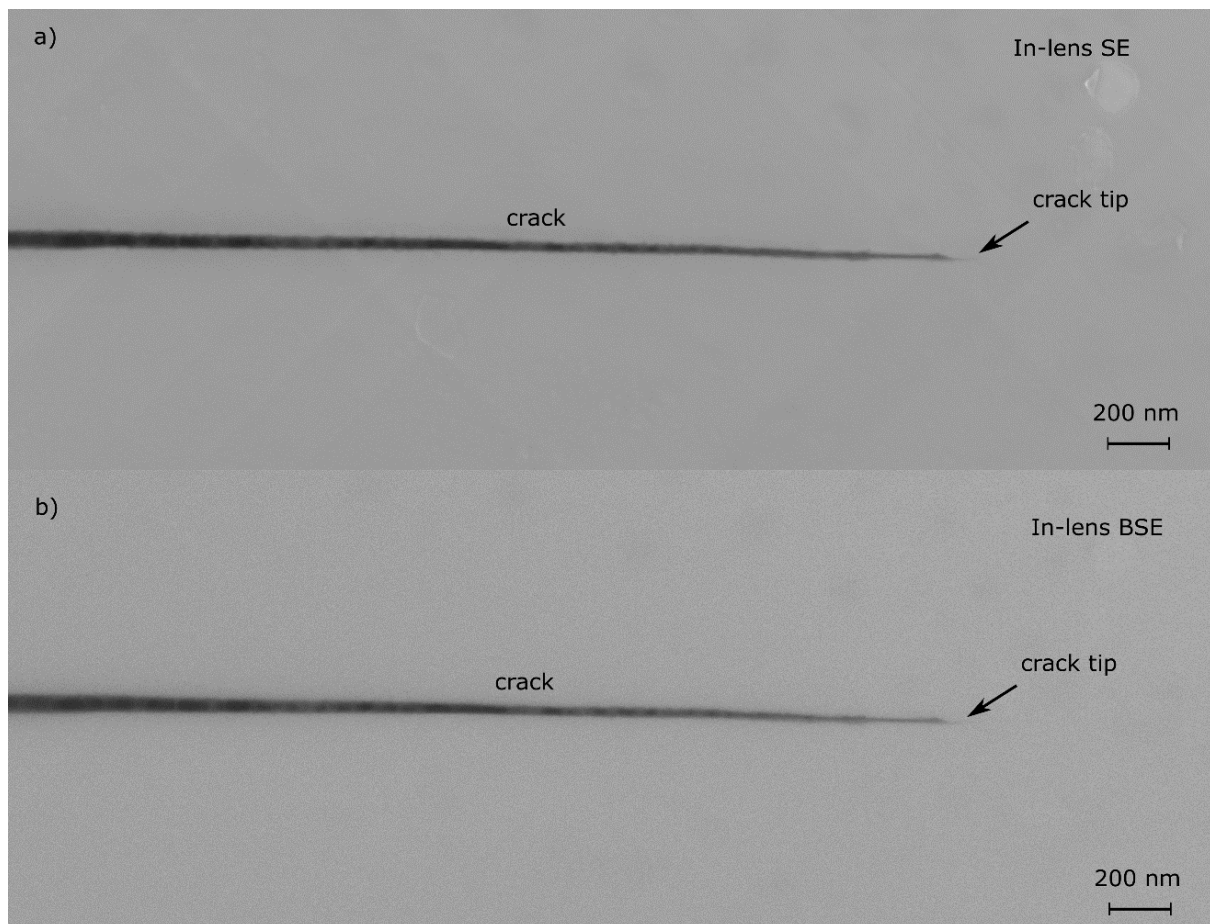


Figure S15: High resolution images of crack tips in MgO at magnification of 100,000 simultaneously using the in-lens SE (a) and the in-lens BSE (b) detector.

Supplementary 17: To verify results in the main text, another material, MgO was tested in related manner

MgO crystals were also purchased from Alineason GmbH (Frankfurt am Main, Germany) and polished with the same respective parameters.

### Nanoindentation:

Nanoindentation was performed with the same parameters with and without dislocation-inducing polishing procedure. As presented in Figure S17, the pop-in stress is eliminated by the high dislocation density in the same manner as in SrTiO<sub>3</sub> which indicated that the conclusions presented in this manuscript can be transferred to other ceramics.

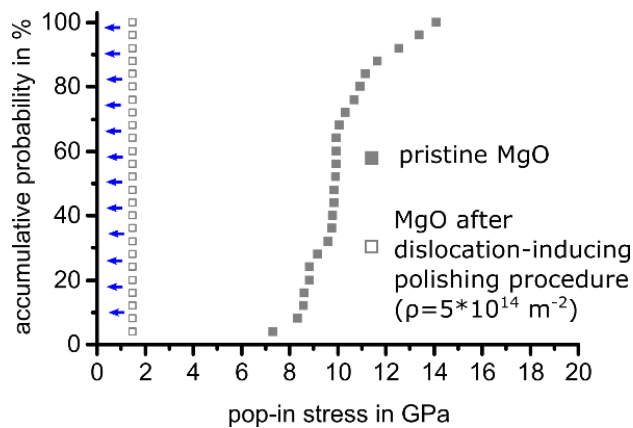
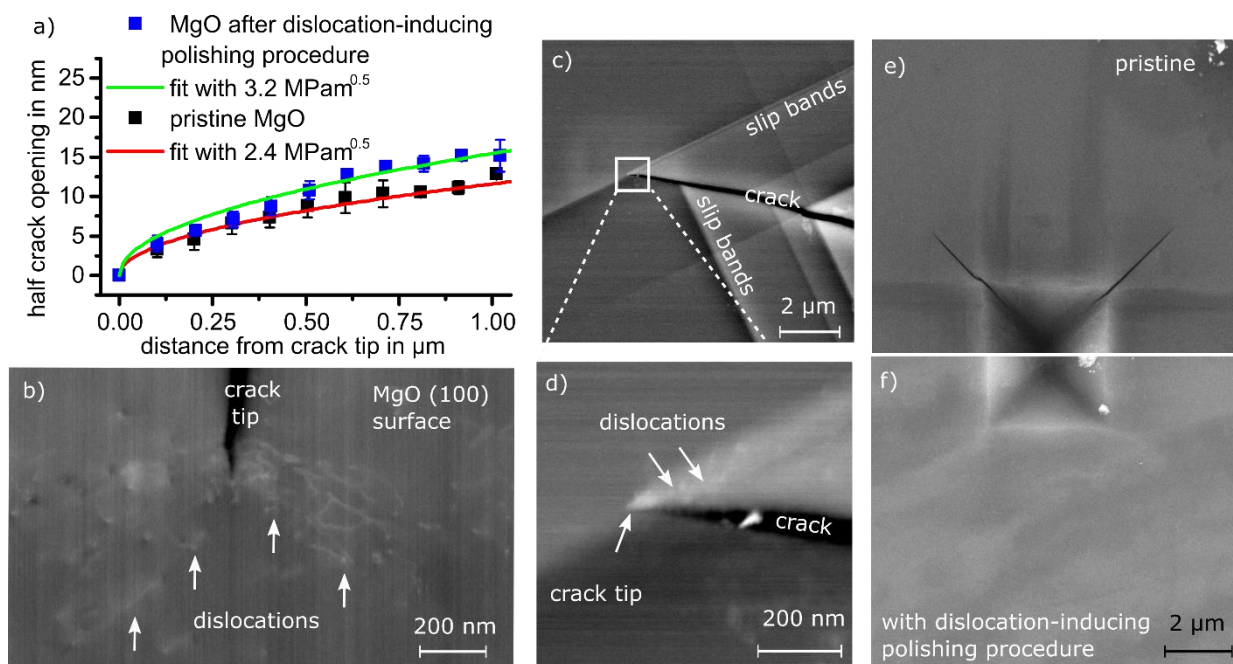


Figure S16: Comparison of pop-in stress of MgO before and after dislocation-inducing polishing procedure. The pop-in stress is eliminated by the high dislocation density in the same manner as in SrTiO<sub>3</sub>.

### Crack tip toughness of MgO:

We also observe an enhancement of the crack tip toughness in MgO by one third when using the dislocation-inducing polishing procedure (Figure S18a). Detailed analysis is, however, complicated by the atypical behavior of MgO where dislocations can be nucleated at low crack velocities<sup>19</sup> providing a crack tip toughness of 2.4 MPa√m while the fracture toughness is below 1 MPa√m for typical crack velocities. Both a plastic zone at crack tips (Figure S18b) and interaction with slip bands (Figure S18c and d) can be observed in pristine crystals. Nevertheless, crack formation can be completely suppressed for 0.1 N indents when applying the dislocation-inducing polishing procedure as illustrated in Figure S18 e and f.



*Figure S17: Interaction of slip bands and crack tip in MgO. a) Determination of the crack tip fracture toughness using crack tip opening displacement averaged over three cracks in pristine samples and three cracks in a sample after applying the dislocation-inducing polishing procedure. b) Electron channeling contrast image revealing a plastic zone around the crack tip in a pristine crystal. c) Image of the interaction between a crack tip with slip bands of a 0.25 N Vickers indent on a (100) surface. d) Magnification of c) featuring individual dislocations. e) Indent on pristine (100) surface of MgO with 0.1 N load. f) Indent on (100) surface of MgO with 0.1 N after dislocation-inducing polishing procedure where cracks are completely suppressed.*

#### Supplementary 18: Avoiding slip band formation by suitable dislocation structures

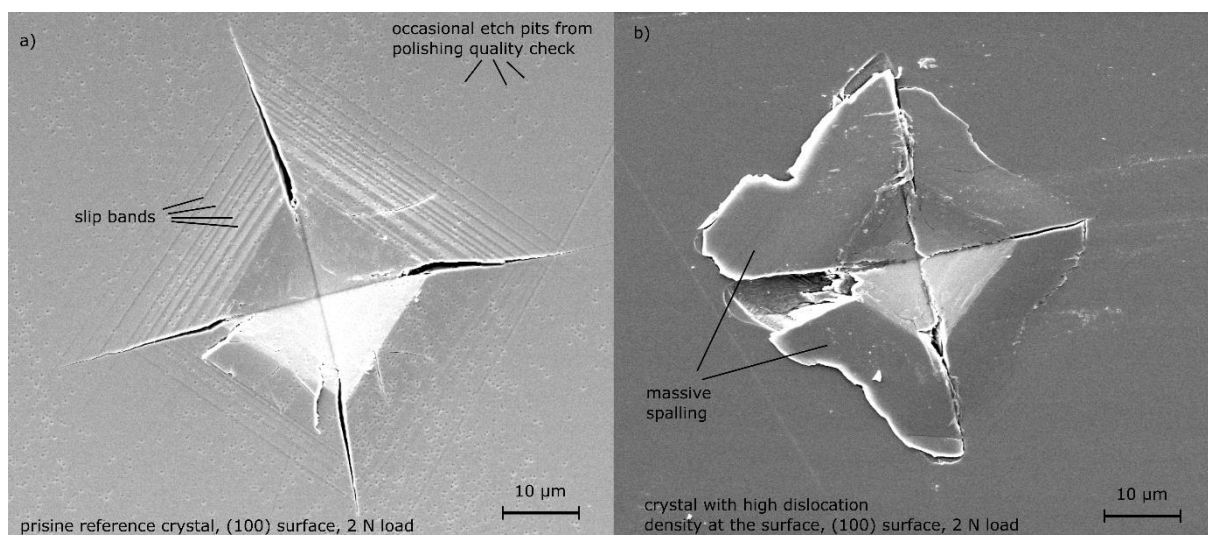


*Figure 18: Comparison of crack formation underneath a 2 N Vickers indent on a pristine (100) surface and on a (100) surface after a dislocation inducing polishing treatment. a) Cracks form along [110] direction from the corners of the Vickers indent where these four cracks are dominating. Furthermore, clear slip bands are visible in the surrounding of the indent. The low natural dislocation density was visualized by etching before indentation. c) Cracking behavior after a dislocation inducing polishing procedure. Cracks also form at the corner, however chipping off (spalling) is dominating over straight cracks. Instead of propagating straight, cracks predominantly propagate underneath the surface. In consequence, the crack is hard to quantify.*

Supplementary 19: Vickers indentation on polycrystals with pristine and enhanced dislocation density at the surface.

SrTiO<sub>3</sub> polycrystals with two different grain sizes have been subjected to the same dislocation-inducing polishing procedure as the single crystals. Vickers indents were made on pristine and dislocation-engineered samples.

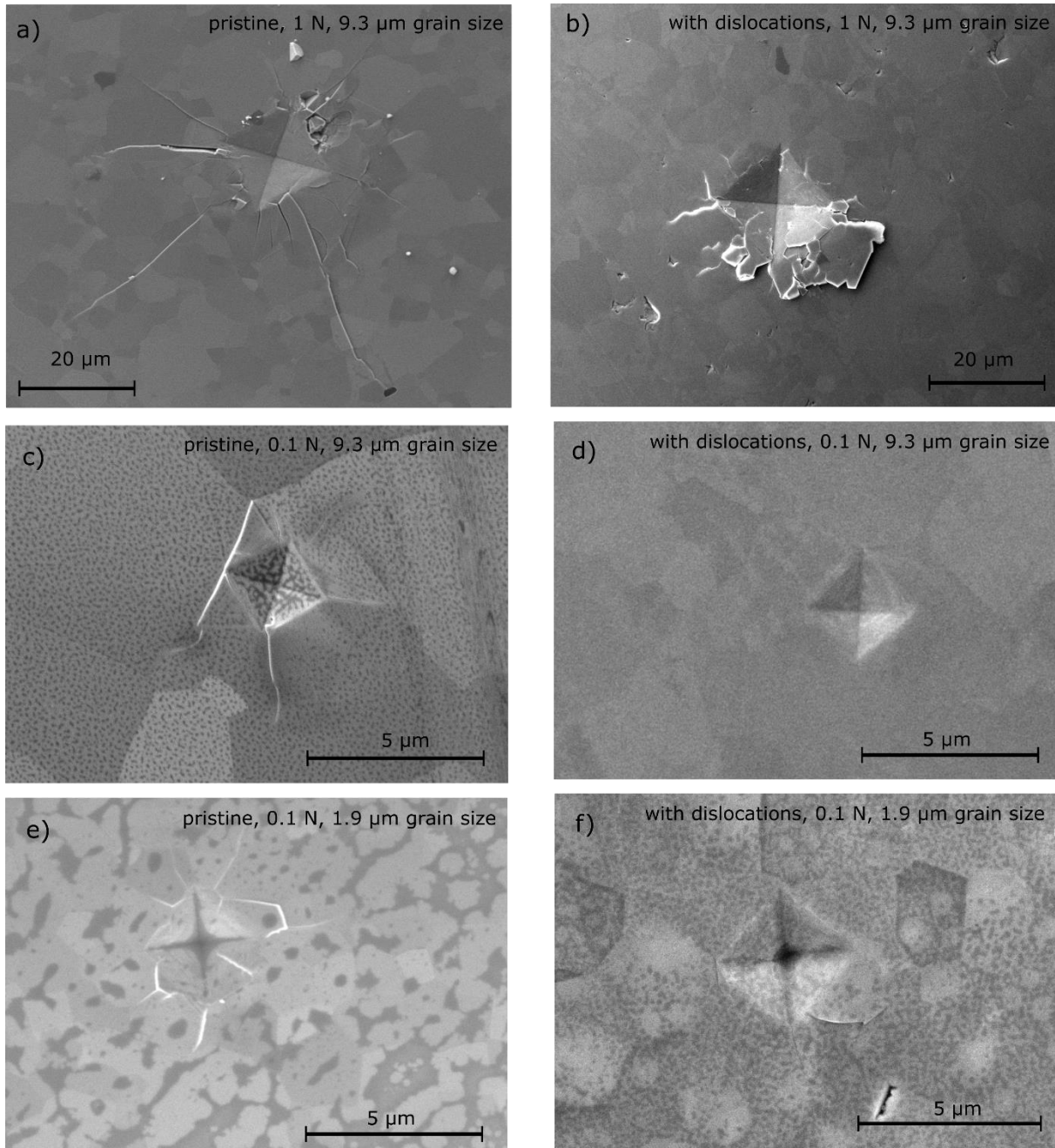


Figure S19: Surface toughening in polycrystals by dislocations. a and b) 1 N Vickers indent on a pristine surface and a surface of a polycrystal after a dislocation-inducing polishing procedure. In the pristine surface, cracks propagate over 30 μm while they are confined to 10 μm in the surface toughened sample. c and d) comparison of a 0.1 N Vickers indent on the same sample as above showing clear cracking for the pristine polycrystal and the absence of cracks in the surface toughened sample. e and f) Same experiment as in c and d but with 1.9 μm grain size instead of 9.3 μm.

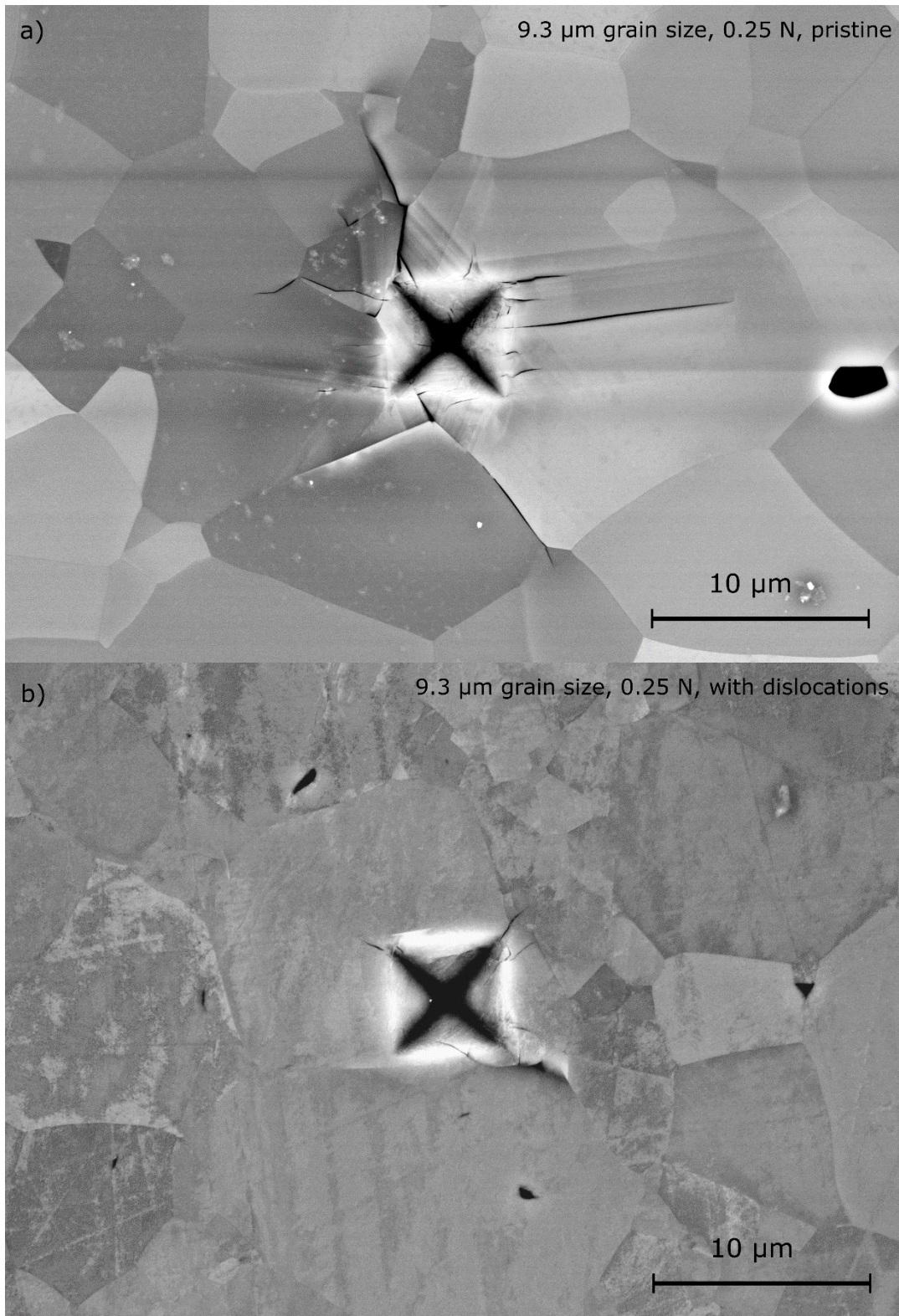


Figure 20: 0.25 N Vickers indents in  $\text{SrTiO}_3$  with 9.3  $\mu\text{m}$  grain size. a) On a pristine surface featuring slip band formation and extensive cracking. b) On a surface after a dislocation inducing polishing procedure marking substantially reduced slip band formation and cracking.

## Supplementary references

1. W. Rheinheimer, M. Baurer, H. Chien, G. S. Rohrer, C. A. Handwerker, J. E. Blendell and M. J. Hoffmann, *Acta Mater.*, 2015, **82**, 32-40.
2. M. Kutsal, P. Bernard, G. Berruyer, P. K. Cook, R. Hino, A. C. Jakobsen, W. Ludwig, J. Ormstrup, T. Roth, H. Simons, K. Smets, J. X. Sierra, J. Wade, P. Wattecamps, C. Yildirim, H. F. Poulsen and C. Detlefs, *40th Riso International Symposium on Materials Science: Metal Microstructures in 2d, 3d and 4d*, 2019, **580**.
3. D. Brunner, S. Taeri-Baghdarani, W. Sigle and M. Rühle, *J. Am. Ceram. Soc.*, 2001, **84**, 1161-1163.
4. P. Hirel, P. Carrez and P. Cordier, *Scripta Mater.*, 2016, **120**, 67-70.
5. L. Porz, T. Frömling, A. Nakamura, N. Li, M. Ryohei, K. Matsunaga, P. Gao, H. Simons, C. Dietz, M. Rohne, J. Janek and J. Rödel, *ACS nano* (in print), 2020, DOI: <https://doi.org/10.1021/acsnano.0c04491>.
6. B. S. Thomas, N. A. Marks and B. D. Begg, *Nucl Instrum Meth B*, 2005, **228**, 288-292.
7. S. Plimpton, *J Comput Phys*, 1995, **117**, 1-19.
8. A. Stukowski, *Modell. Simul. Mater. Sci. Eng.*, 2010, **18**, 015012.
9. A. Stukowski, V. V. Bulatov and A. Arsenlis, *Modell. Simul. Mater. Sci. Eng.*, 2012, **20**, 085007.
10. A. H. Cottrell, *Prog Met Phys*, 1953, **4**, 205-264.
11. J. Marian, W. Cai and V. V. Bulatov, *Nat Mater*, 2004, **3**, 158-163.
12. P. Hirel, P. Marton, M. Mrovec and C. Elsässer, *Acta Mater.*, 2010, **58**, 6072-6079.
13. D. Marrocchelli, L. X. Sun and B. Yildiz, *J. Am. Chem. Soc.*, 2015, **137**, 4735-4748.
14. K. L. Johnson, *Contact Mechanics*, Cambridge University Press, Cambridge, London, 1985.
15. E. A. M. Patterson, Marton; Donner, Wolfgang; Durst, Karsten; Webber, Kyle G.; Rödel, Jürgen, *J. Am. Ceram. Soc.*, 2016, **99**, 3411-3420.
16. J. Seidel and J. Rödel, *J. Am. Ceram. Soc.*, 1997, **80**, 433-438.
17. F. Haubensak and A. S. Argon, *J Mater Sci*, 1997, **32**, 1473-1477.
18. R. O. Silva, J. Malzbender, F. Schulze-Koppers, S. Baumann and O. Guillon, *J. Eur. Ceram. Soc.*, 2017, **37**, 2629-2636.
19. J. L. Robins, T. N. Rhodin and R. L. Gerlach, *J. Appl. Phys.*, 1966, **37**, 3893-3903.